J|A|C|S
ARTICLES
Published on Web 08/06/2005

# Unique CO Chemisorption Properties of Gold Hexamer: $Au_6(CO)_n^-$ ($n = 0-3$)

Hua-Jin Zhai,[†] Boggavarapu Kiran,[†] Bing Dai,[†] Jun Li,[‡] and Lai-Sheng Wang*,[†]

*Contribution from the Department of Physics, Washington State University, 2710 University Drive, Richland, Washington 99352, and W. R. Wiley Environmental Molecular Sciences Laboratory and Chemical Sciences Division, Pacific Northwest National Laboratory, P.O. Box 999, Richland, Washington 99352*

Received April 21, 2005; E-mail: ls.wang@pnl.gov

***Abstract:*** Elucidating the chemisorption properties of CO on gold clusters is essential to understanding the catalytic mechanisms of gold nanoparticles. Gold hexamer $Au_6$ is a highly stable cluster, known to possess a $D_{3h}$ triangular ground state structure with an extremely large HOMO−LUMO gap. Here we report a photoelectron spectroscopy (PES) and quasi-relativistic density functional theory (DFT) study of $Au_6$−CO complexes, $Au_6(CO)_n^-$ and $Au_6(CO)_n$ ($n = 0-3$). CO chemisorption on $Au_6$ is observed to be highly unusual. While the electron donor capability of CO is known to decrease the electron binding energies of $Au_m(CO)_n^-$ complexes, CO chemisorption on $Au_6$ is observed to have very little effect on the electron binding energies of the first PES band of $Au_6(CO)_n^-$ ($n = 1-3$). Extensive DFT calculations show that the first three CO successively chemisorb to the three apex sites of the $D_{3h}$ $Au_6$. It is shown that the LUMO of the $Au_6$−CO complexes is located in the inner triangle. Thus CO chemisorption on the apex sites (outer triangle) has little effect on this orbital, resulting in the roughly constant electron binding energies for the first PES band in $Au_6(CO)_n^-$ ($n = 0-3$). Detailed molecular orbital analyses lead to decisive information about chemisorption interactions between CO and a model Au cluster.

## 1. Introduction

The discovery of remarkable catalytic activities of highly dispersed gold nanoparticles for low-temperature CO oxidation as pioneered by Haruta et al.[1] has stimulated considerable research on gold clusters.[2] Because of their potentials for industrial applications, extensive research efforts have been directed at the elucidation of the catalytic mechanisms of nanogold.[3−13] Different models have been proposed, including the perimeter sites model,[2] the nonmetallic gold model,[3] the extra electron model,[11] and the low-coordination sites model.[8,13] However, the exact catalytic mechanisms are still being debated.[2,13,14] Size-selected cluster deposition studies[11,12] and gas-phase experimental[15−23] and theoretical[24−30] studies have

[†] Washington State University and Pacific Northwest National Laboratory.
[‡] Pacific Northwest National Laboratory.

(1) Haruta, M.; Yamada, N.; Kobayashi, T.; Iijima, S. *J. Catal*. **1989**, *115*, 301. Haruta, M.; Tsubota, S.; Kobayashi, T.; Kageyama, H.; Genet, M. J.; Delmon, B. *J. Catal*. **1993**, *144*, 175.
(2) For recent reviews, see: Haruta, M. *Catal. Today* **1997**, *36*, 153. Haruta, M. *Chem. Rec*. **2003**, *3*, 75. Bond, G. C.; Thompson, D. T. *Catal. Rev. Sci. Eng*. **1999**, *41*, 319.
(3) Valden, M.; Lai, X.; Goodman, D. W. *Science* **1998**, *281*, 1647. Chen, M. S.; Goodman, D. W. *Science* **2004**, *306*, 252.
(4) Iizuka, Y.; Tode, T.; Takao, T.; Yatsu, K. I.; Takeuchi, T.; Tsubota, S.; Haruta, M. *J. Catal*. **1999**, *187*, 50.
(5) Kim, T. S.; Stiehl, J. D.; Reeves, C. T.; Meyer, R. J.; Mullins, C. B. *J. Am. Chem. Soc*. **2003**, *125*, 2018. Stiehl, J. D.; Kim. T. S.; McClure S. M.; Mullins, C. B. *J. Am. Chem. Soc*. **2004**, *126*, 1606.
(6) Guzman, J.; Gates, B. C. *Nano Lett.* **2001**, *1*, 689. Guzman, J.; Gates, B. C. *J. Am. Chem. Soc*. **2004**, *126*, 2672.
(7) Date, M.; Okumura, M.; Tsubota, S.; Haruta, M. *Angew.* Chem., Int. Ed. **2004**, *43*, 2129.
(8) Lemire, C.; Meyer, R.; Shaikhutdinov, S.; Freund, H. J. *Angew.* Chem., Int. Ed. **2004**, *43*, 118.
(9) Liu, Z. P.; Hu, P.; Alavi, A. *J. Am. Chem. Soc*. **2002**, *124*, 14770.
(10) Molina, L. M.; Hammer, B. *Phys. Rev. Lett*. **2003**, *90*, 206102.
(11) Sanchez, A.; Abbet, S.; Heiz. U.; Schneider, W. D.; Hakkinen, H.; Barnett, R. N.; Landman, U. *J. Phys. Chem. A* **1999**, *103*, 9573. Yoon, B.; Hakkinen, H.; Landman, U.; Wirz, A. S.; Antonietti, J. M.; Abbet, S.; Heiz, U. *Science* **2005**, *307*, 403.
(12) Lee, S.; Fan, C.; Wu, T.; Anderson, S. L. *J. Am. Chem. Soc*. **2004**, *126*, 5682.
(13) Mavrikakis, M.; Stoltze, P.; Norskov, J. K. *Catal. Lett.* **2000**, *64*, 101. Lopez, N.; Janssens, T. V. W.; Clausen, B. S.; Xu, Y.; Mavrikakis, M.; Bligaard, T.; Norskov, J. K. *J. Catal*. **2004**, *223*, 232.
(14) Cho, A. *Science* **2003**, *299*, 1684.
(15) Stolcic, D.; Fischer, M.; Gantefor, G.; Kim, Y. D.; Sun, Q.; Jena, P. *J. Am. Chem. Soc*. **2003**, *125*, 2848. Sun, Q.; Jena, P.; Kim, Y. D.; Fischer, M.; Gantefor, G. *J. Chem. Phys*. **2004**, *120*, 6510.
(16) Kimble, M. L.; Castleman, Jr., A. W.; Mitric, R.; Burgel, C.; Bonacic-Koutecky, V. *J. Am. Chem. Soc*. **2004**, *126*, 2526.
(17) Hagen, J.; Socaciu, L. D.; Elijazyfer, M.; Heiz, U.; Bernhardt, T. M.; Woste, L. *Phys. Chem. Chem. Phys*. **2002**, *4*, 1707. Socaciu, L. D.; Hagen, J.; Bernhardt, T. M.; Woste, L.; Heiz, U.; Hakkinen, H.; Landman, U. *J. Am. Chem. Soc*. **2003**, *125*, 10437.
(18) Wallace, W. T.; Whetten, R. L. *J. Am. Chem. Soc*. **2002**, *124*, 7499.
(19) Nygren, M. A.; Siegbahn, P. E. M.; Jin, C.; Guo, T.; Smalley, R. E. *J. Chem. Phys.* **1991**, *95*, 6181.
(20) Lee, T. H.; Ervin, K. M. *J. Phys. Chem.* **1994**, *98*, 10023.
(21) Wallace, W. T.; Whetten, R. L. *J. Phys. Chem. B* **2000**, *104*, 10964.
(22) Balteanu, I.; Balaj, O. P.; Fox, B. S.; Beyer, M. K.; Bastl, Z.; Bondybey, V. E. *Phys. Chem. Chem. Phys*. **2003**, *5*, 1213.
(23) Liang, B.; Andrews, L. *J. Phys. Chem. A* **2000**, *104*, 9156. Liang, L.; Xu, Q. *J. Phys. Chem. A* **2005**, *109*, 1026.
(24) Yoon, B.; Hakkinen, H.; Landman, U. *J. Phys. Chem. A* **2003**, *107*, 4066.
(25) Varganov, S. A.; Olson, R. M.; Gordon, M. S.; Meitu, H. *J. Chem. Phys*. **2003**, *119*, 2531. Varganov, S. A.; Olson, R. M.; Gordon, M. S.; Mills, G.; Meitu, H. *Chem. Phys. Lett*. **2003**, *368*, 778. Mills, G.; Gordon, M. S.; Meitu, H. *Chem. Phys. Lett*. **2002**, *359*, 493.
(26) Ding, X.; Li, Z.; Yang, J.; Hou, J. G.; Zhu, Q. *J. Chem. Phys*. **2004**, *120*, 9594.
(27) Wu, X.; Senapati, L.; Nayak, S. K.; Selloni, A.; Hajaligol, M. *J. Chem. Phys*. **2002**, *117*, 4010.
(28) Yuan, D. W.; Zeng, Z. *J. Chem. Phys*. **2004**, *120*, 6574.
(29) Hakkinen, H.; Landman, U. *J. Am. Chem. Soc*. **2001**, *123*, 9704.

 **10.1021/ja052618k CCC: $30.25** 

been carried out to model this catalytic reaction in a well-controlled manner, providing fundamental mechanistic information at the molecular level. Chemisorbed gold cluster complexes serve as ideal model systems for nanogold catalysts, even though the role of substrates cannot be addressed.[31] Numerous mass spectrometric,[19] photoelectron spectroscopic,[15] and density functional theory (DFT)[15,25,26,29] studies have established that $O_2$ adsorbs on gold clusters molecularly. Evidence for molecular chemisorption of $O_2$ on $TiO_2$-supported gold nanoparticles has also been observed recently.[5] Coadsorption of CO and $O_2$ on small gold clusters has been investigated by mass-spectrometry-based experiments, and it was revealed that CO and $O_2$ adsorb cooperatively, rather than competitively.[17,18]

However, little experimental information is available on how CO molecules interact with gold clusters and gold nanoparticles.[19−23] Chemical reactions of gold clusters with CO have been studied,[19−22] and pronounced size dependence and saturation were observed. Infrared spectra of Au−CO complexes formed in a rare gas matrix have been reported,[23] and complexes such as $Au(CO)_n$ ($n = 1-5$) and $Au_n(CO)_2$ ($n = 1, 2$) were assigned. However, definitive electronic and structural information on the $Au_m(CO)_n$ complexes is still elusive. Such information would be valuable in the mechanistic understanding for the catalytic CO oxidation by gold nanoparticles.

In a recent communication,[32] we reported the generation of several series of gold carbonyl cluster anions $Au_m(CO)_n^-$ ($m = 2-5$, $n = 1-7$) in the gas phase and characterized their electronic structure using photoelectron spectroscopy (PES). We observed that the first few CO groups induce significant red shifts to the photoelectron spectra, suggesting that CO acts as electron donors to the gold clusters. For a given gold cluster, CO adsorption reaches a critical number, beyond which further CO adsorption changes the spectra very little. The critical CO numbers correspond exactly to the available low coordination apex sites on the respective bare gold clusters. It was suggested that CO first chemisorbs to the apex sites and additional CO then only physisorbs to the chemisorption-saturated $Au_m(CO)_n^-$ complexes. The observation that CO chemisorption induces significant decreases to the electron binding energies of the $Au_m(CO)_n^-$ complexes is important, suggesting that CO chemisorption would promote $O_2$ adsorption because the latter involves electron transfers from the cluster. Thus the previous experimental results provided electronic and spectroscopic basis for the cooperative chemisorption of CO and $O_2$ on gold clusters and may hold the key for the mechanistic understanding of nanogold catalysts for CO oxidation. However, a detailed molecular understanding about how CO interacts with gold is still lacking.

In the current paper, we report a combined PES and DFT investigation of the CO chemisorption behavior on the gold hexamer from one to three CO groups, $Au_6(CO)_n^-$ ($n = 0-3$). Bare gold hexamer has unique electronic and structural properties.[33−36] Structurally, $Au_6$ and $Au_6^-$ were well-characterized to possess a close-packed planar triangular structure with $D_{3h}$ symmetry.[36] This highly symmetric structure, stabilized by strong relativistic effects,[37] aromaticity, and aurophilic attraction,[38] may be viewed as a small piece of Au(111) surface or an ideal model catalytic surface composed of apex and edge sites only. Electronically, $Au_6$ is known to possess the largest HOMO−LUMO gap among gold clusters[34,35] and has been proposed to be a six-electron magic cluster within a two-dimensional electronic shell model.[39] Upon CO chemisorption, we observed surprisingly that the first three CO chemisorptions do not significantly change the electron binding energies of the first PES band in $Au_6(CO)_n^-$ ($n = 1-3$), in direct contrast to our previous study on the smaller $Au_m(CO)_n^-$ ($m = 2-5$) complexes. Only the binding energies of the second PES band in $Au_6(CO)_n^-$ were observed to be red-shifted, resulting in a closing of the HOMO−LUMO gaps upon CO chemisorption. We also performed extensive quasi-relativistic DFT calculations to examine chemisorption structures in $Au_6(CO)_n^-$ and $Au_6(CO)_n$ ($n = 1-3$). We found that the first three CO successively chemisorb to the apex sites of the triangular $Au_6$ without significantly perturbing the parent $Au_6$ structure. The unique CO chemisorption behavior and its influence on the electronic structure of $Au_6$ are understood using molecular orbital analysis, providing detailed information about the molecular and electronic interactions between CO and $Au_6$.

## 2. Experimental and Computational Methods

**2.1. Photoelectron Spectroscopy.** The experiments were carried out using a magnetic-bottle-type PES apparatus equipped with a laser vaporization supersonic cluster source, details of which were described elsewhere.[40] Briefly, $Au_m(CO)_n^-$ cluster anions were produced by laser vaporization of a pure gold target in the presence of a helium carrier gas seeded with 2% CO. Various $Au_m(CO)_n^-$ clusters were generated and mass-analyzed using a time-of-flight mass spectrometer. The $Au_6(CO)_n^-$ ($n = 1-3$) species were each mass-selected and decelerated before being photodetached. Three detachment photon energies were used in the current study: 532 nm (2.331 eV), 266 nm (4.661 eV), and 193 nm (6.424 eV). Photoelectrons were collected at nearly 100% efficiency by the magnetic bottle and analyzed in a 3.5 m long electron flight tube. The PES spectra were calibrated using the known spectra of $Au^-$ and $Rh^-$, and the energy resolution of the apparatus was $\Delta E_k/E_k \sim 2.5\%$, that is, $\sim$25 meV for 1 eV electrons.

(30) Lopez, N.; Norskov, J. K. *J. Am. Chem. Soc.* **2002**, *124*, 11262.
(31) While oxide support is observed to play important roles in nanogold catalysis (ref 2), there is accumulating evidence that the size of nanogold overwhelmingly determines the catalytic activity (refs 2 and 13). Nanogold is an active catalyst even without oxide support (ref 4), which justifies chemisorbed gold cluster complexes as molecular models for mechanistic understanding of nanogold catalysts.
(32) Zhai, H. J.; Wang, L. S. *J. Chem. Phys.* **2005**, *122*, 051101.
(33) Furche, F.; Ahlrichs, R.; Wies, P.; Jacob, C.; Gilb, S.; Bierweiler, T.; Kappes, M. M. *J. Chem. Phys.* **2002**, *117*, 6982.
(34) Hakkinen, H.; Yoon, B.; Landman, U.; Li, X.; Zhai, H. J.; Wang, L. S. *J. Phys. Chem. A* **2003**, *107*, 6168.
(35) Taylor, K. J.; Jin, C.; Conceicao, J.; Wang, L. S.; Cheshnovsky, O.; Johnson, B. R.; Nordlander, P. J.; Smalley, R. E. *J. Chem. Phys.* **1990**, *93*, 7515. Taylor, K. J.; Pettiette-Hall, C. L.; Cheshnovsky, O.; Smalley, R. E. *J. Chem. Phys.* **1992**, *96*, 3319. Gantefor, G.; Cox, D. M.; Kaldor, A. *J. Chem. Phys.* **1992**, *96*, 4102. Liao, D. W.; Balasubramanian, K. *J. Chem. Phys.* **1992**, *97*, 2548.
(36) Bravo-Perez, G.; Novaro, O. *Chem. Phys. Lett.* **1999**, *313*, 655. Hakkinen, H.; Landman, U. *Phys. Rev. B* **2000**, *62*, R2287. Wang, J.; Wang, G.; Zhao, J. *Phys. Rev. B* **2002**, *66*, 035418. Bonacic-Koutecky, V.; Burda, J.; Mitric, R.; Ge, M.; Zampella, G.; Fantucci, P. *J. Chem. Phys.* **2002**, *117*, 3120. Lee, H. M.; Ge, M.; Sahu, B. R.; Tarakeshwar, P.; Kim, K. S. *J. Phys. Chem. B* **2003**, *107*, 9994. Fernandez, E. M.; Soler, J. M.; Garzon, I. L.; Balbas, L. C. *Phys. Rev. B* **2004**, *70*, 165403. Xiao, L.; Wang, L. C. *Chem. Phys. Lett.* **2004**, *392*, 452. Remacle, F.; Kryachko, E. S. *J. Chem. Phys.* **2005**, *122*, 044304. Olson, R. M.; Varganov, S.; Gordon, M. S.; Meitu, H.; Chretien, S.; Piecuch, P.; Kowalski, K.; Kucharski, S. A.; Musial, M. *J. Am. Chem. Soc.* **2005**, *127*, 1049.
(37) Pyykko, P. *Chem. Rev.* **1988**, *88*, 563.
(38) Schmidbaur, H. *Gold Bull.* (*London*) **2000**, *33*, 3.
(39) Tanaka, H.; Neukermans, S.; Janssens, E.; Silverans, R. E.; Lievens, P. *J. Am. Chem. Soc.* **2003**, *125*, 2862. Janssens, E.; Tanaka, H.; Neukermans, S.; Silverans, R. E.; Lievens, P. *New. J. Phys.* **2003**, *5*, 46.
(40) Wang, L. S.; Cheng, H. S.; Fan, J. *J. Chem. Phys.* **1995**, *102*, 9480. Wang, L. S.; Wu, H. B. In *Advances in Metal and Semiconductor Clusters. IV. Cluster Materials*; Duncan, M. A., Ed.; JAI Press: Greenwich, CT, 1998; pp 299−343.

**2.2. Density Functional Calculations.** In the DFT calculations, we used the Stuttgart 19-valence-electron energy-consistent pseudopotentials[41] and basis sets augmented with two f-type and one g-type polarization functions ($\zeta_f = 0.498$, 1.461, and $\zeta_g = 1.218$) for gold as recommended by Martin and Sundermann[42] and Dunning's all-electron basis set aug-cc-pVTZ for oxygen and carbon.[43] Scalar (mass-velocity and Darwin) relativistic effects were taken into account via the quasi-relativistic pseoudopotentials. A variety of exchange-correlation functionals were tested for accuracy and consistency. We found that the B3LYP hybrid functional, which makes use of the Hartree−Fock exact exchange and Becke's exchange functional and Lee−Yang−Parr correlation functional,[44] gave electron binding energies in good agreement with the experimental data. Harmonic frequency calculations were performed to verify that the obtained structures are minima on the potential energy surfaces. All calculations were spin-restricted for closed-shell molecules and spin-unrestricted for open-shell species. Adiabatic detachment energies (ADEs) were calculated via the total energy difference (i.e., ΔSCF method), whereas the vertical detachment energies (VDEs) for the anionic clusters were calculated using the combined ΔSCF-TDDFT approach.[45,46] For all calculations, the extra fine integration grid was used to obtain highly accurate DFT results. All calculations were accomplished using the NWChem 4.6 program and the Molecular Science Computing Facility located at the Environmental Molecular Sciences Laboratory.[47] Molecular orbitals were visualized using GaussView 3.0.[48]

## 3. Experimental Results

The PES spectra of $Au_6(CO)_n^-$ ($n = 0-3$) were obtained at three detachment photon energies (532, 266, and 193 nm). Figure 1 compares the 193 nm spectra of all the species. The spectra at all three photon energies are given as Supporting Information in Figures S1−S4. The lower photon energy spectra had better spectral resolution and yielded more accurate ADEs and VDEs, which are summarized in Table 1 for the first two detachment features (bands X and A in Figure 1). Since no vibrational structures were resolved in the PES data, the ADEs, that is, the electron affinities of the corresponding neutral clusters, were evaluated by drawing a straight line at the leading edge of the ground-state feature X and then adding the instrumental resolution to the intersections with the binding energy axis. Although this is an approximate procedure, we were able to obtain consistent ADEs from spectra taken at different photon energies due to the relatively sharp onset of the data. The VDE differences between bands A and X give approximately the experimental measures for the HOMO−LUMO gap of the neutral complexes and are given in Table 2. The VDE and ADE difference of band X defines the reorganization energy (Table 2), which is a measure of the geometry changes between the anion and neutral ground states. The VDEs for all the observed features for each species are given as Supporting Information in Tables S1−S4, where the calculated VDEs are also listed (see below).

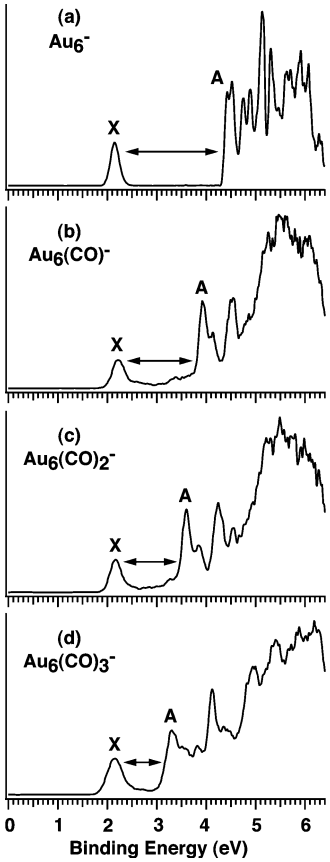


***Figure 1.*** Photoelectron spectra of $Au_6(CO)_n^-$ ($n = 0-3$) at 193 nm. The arrows indicate the observed energy gaps.

***Table 1.*** Observed Adiabatic and Vertical Detachment Energies from the Photoelectron Spectra of $Au_6(CO)_n^-$ ($n = 0-3$), and Comparison with Theoretical Detachment Energies[a]

| | exptl[b,c] | | | theor[b,d] | | |
|---|---|---|---|---|---|---|
| | feature | ADE | VDE | ADE | state (MO) | VDE |
| $Au_6^-$ | X | 2.06 (2) | 2.13 (2) | 2.02 | $^1A_1'$ ($6a_1'$) | 2.12 |
| | A | | 4.43 (2) | | $^3E'$ ($7e'$) | 4.43 |
| $Au_6(CO)^-$ | X | 2.04 (5) | 2.20 (3) | 2.10 | $^1A_1$ ($11b_2$) | 2.26 |
| | A | | 3.92 (2) | | $^3B_2$ ($15a_1$) | 3.91 |
| $Au_6(CO)_2^-$ | X | 2.03 (5) | 2.15 (3) | 2.16 | $^1A_1$ ($17a_1$) | 2.30 |
| | A | | 3.60 (2) | | $^3B_2$ ($13b_2$) | 3.75 |
| $Au_6(CO)_3^-$ | X | 1.95 (5) | 2.15 (3) | 1.86 | $^1A_1$ ($20a_1$) | 2.15 |
| | A | | 3.32 (3) | | $^3B_2$ ($14b_2$) | 3.53 |

[a] For complete data sets, see Supporting Information Tables S1−S4. [b] All detachment energies are in eV. [c] The ground-state ADE also represents the electron affinity of the corresponding neutral species. [d] "State (MO)" denotes the final neutral triplet and singlet states upon electron detachment from the corresponding molecular orbital of the anion.

***Table 2.*** Comparison of Experimental and Theoretical X−A Energy Gaps and Reorganization Energies of $Au_6(CO)_n^-$ ($n = 0-3$)

| | energy gap[a] | | reorganization energy[a] | |
|---|---|---|---|---|
| | exptl[b] | theor | exptl[b] | theor |
| $Au_6^-$ | 2.30 | 2.31 | 0.07 | 0.10 |
| $Au_6(CO)^-$ | 1.72 | 1.65 | 0.16 | 0.16 |
| $Au_6(CO)_2^-$ | 1.45 | 1.45 | 0.12 | 0.14 |
| $Au_6(CO)_3^-$ | 1.17 | 1.38 | 0.20 | 0.29 |

[a] All energies are in eV. [b] The estimated uncertainty is ±0.03 eV.

(41) Andrae, D.; Häusserman, U.; Dolg, M.; Stoll, H.; Preuss, H.; *Theor. Chim. Acta* **1990**, *77*, 123.
(42) Martin, J. M. L.; Sundermann, A. *J. Chem. Phys.* **2001**, *114*, 3408.
(43) Dunning, T. H., Jr. *J. Chem. Phys.* **1989**, *90*, 1007. Kendall, R. A.; Dunning, T. H., Jr.; Harrison, R. J. *J. Chem. Phys.* **1992**, *96*, 6796.
(44) Becke, A. D. *J. Chem. Phys.* **1993**, *98*, 1372/5648. Lee, C.; Yang, G.; Parr, R. G. *Phys. Rev. B* **1988**, *37*, 785. Stephens, P. J.; Devlin, F. J.; Chabalowski, C. F.; Frisch, M. J. *J. Phys. Chem.* **1994**, *98*, 11623. P. J. Stephens, F. J. Devlin, C. S. Ashvar, C. F. Chabalowski, and M. J. Frisch, *Faraday Discuss.* **1994**, *99*, 103.
(45) Casida, M. E.; Jamrski, C.; Casida, K. C.; Salahaub, D. R. *J. Chem. Phys.* **1998**, *108*, 4439.
(46) Li, J.; Li, X.; Zhai, H. J.; Wang, L. S. *Science* **2003**, *299*, 864.
(47) *NWChem, A Computational Chemistry Package for Parallel Computers, Version 4.6*; Pacific Northwest National Laboratory: Richland, Washington, USA, 2004.
(48) *GaussView 3.0*; Gaussian, Inc., Carnegie Office Park, Building 6, Pittsburgh, PA 15106, USA. Copyright©2000−2003, Semichem, Inc.

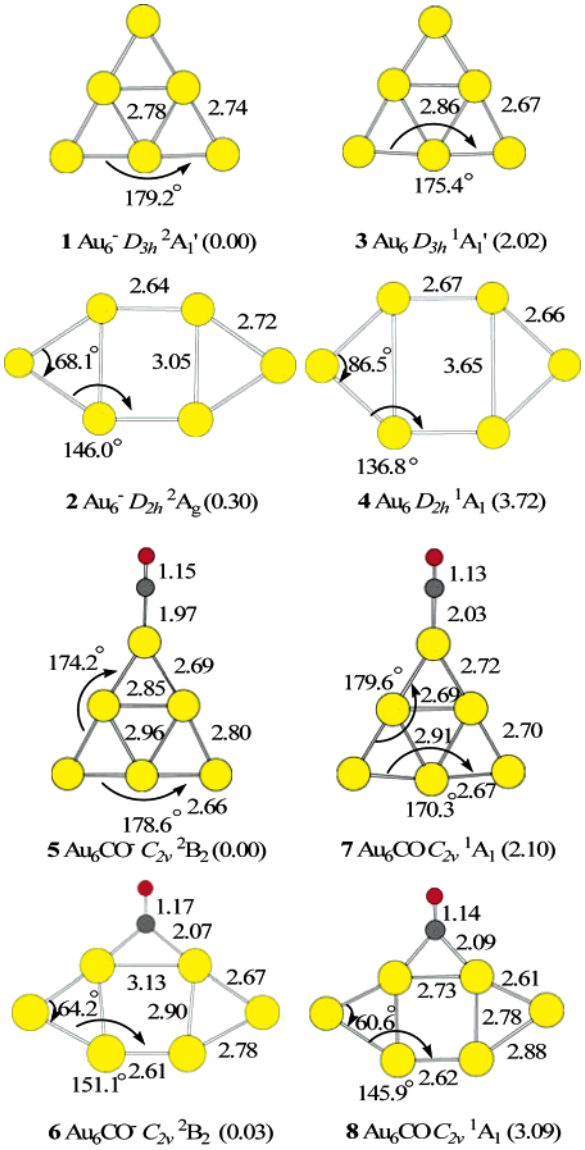


***Figure 2.*** Optimized structures of the ground state and a low-lying isomer for $Au_6^-$, $Au_6(CO)^-$, and their corresponding neutrals. All bond lengths are in Å, and all relative energies (in eV) are referenced to the anion ground state.

Well-resolved PES spectra for $Au_6^-$ were presented in our previous work.[34] The ADE and VDE of the ground-state X were measured to be 2.06 and 2.13 eV, respectively, where the ADE is in good agreement with a previous ZEKE measurement (2.05 eV).[35] The VDE of band A at 4.43 eV defines an extremely large HOMO−LUMO gap of 2.30 eV for neutral $Au_6$, which is the largest among all gold clusters.[34,35] Upon adsorption of the first CO, the ground state feature X broadened (Figure 1b), but its binding energies (ADE: 2.04 eV; VDE: 2.20 eV) showed very little change relative to that of the bare cluster. This is completely different from the chemisorption behavior of the smaller gold clusters, where a red shift of as much as 0.6 to 0.7 eV was observed upon the first CO chemisorption for $Au_n^-$ ($n$ = 2−5).[32] However, the second VDE, corresponding to electron detachment from the anion ground state to the first neutral excited state (A), was measured to be 3.92 eV, significantly red-shifted by 0.51 eV with respect to that of $Au_6^-$ and resulting in a much smaller X−A energy gap (1.72 eV).

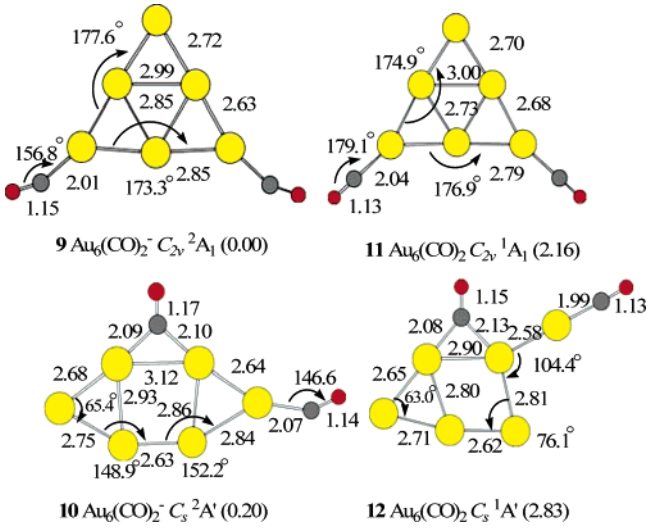


***Figure 3.*** Optimized structures of the ground state and a low-lying isomer for $Au_6(CO)_2^-$ and $Au_6(CO)_2$. All bond lengths are in Å, and all relative energies (in eV) are referenced to the anion ground state.

Upon further CO adsorption, the overall spectral patterns of $Au_6(CO)_2^-$ (Figure 1c) and $Au_6(CO)_3^-$ (Figure 1d) appeared similar to that of $Au_6(CO)^-$: the first PES band X showed very little dependence on the number of CO ligands, whereas the higher binding energy features displayed continued red shifts, resulting in smaller and smaller X−A energy gaps: 1.45 eV for $Au_6(CO)_2^-$ and 1.17 eV for $Au_6(CO)_3^-$. Very weak signals were observed in the X−A gap region in the spectra of the CO chemisorbed species (Figure 1). These weak signals were likely due to minor structural isomers in the CO-chemisorbed complexes. Stronger signals were observed in the X−A gap region in the 266 nm spectra (Figures S2−S4). In fact, weak signals were also present in the 266 nm spectrum of the bare $Au_6^-$ (Figure S1b). These enhanced signals in the X−A gap region in the chemisorbed species at 266 nm were most likely due to autodetachment, which has been observed in other clusters with large HOMO−LUMO gaps, in particular for $C_{60}^-$ and $Au_{20}^-$.[46,49]

## 4. Computational Results

To find the CO chemisorption sites on the gold hexamer, we searched a variety of isomers for $Au_6(CO)_n$ and $Au_6(CO)_n^-$ ($n$ = 0−3). Optimized ground state and selected low-lying isomers for $Au_6(CO)_n$ and $Au_6(CO)_n^-$ (**1**−**18**) are presented in Figures 2−4. Optimized structures for other isomers and their relative energies are presented as Supporting Information in Figures S5−S7. The computed ADEs for the ground state and computed VDEs for the ground and first excited states of the lowest energy isomers are compared with the experimental data in Table 1. The computed VDEs for all the detachment channels up to the 193 nm photon energy for the global minimum structures are given in Tables S1−S4. On the basis of these computed VDEs, we simulated the photoelectron spectra by convoluting each vertical detachment energy with a Gaussian function, as shown in Figure 5. In addition, the CO chemisorption energies were also computed, as compared with previous DFT results[27,28] in Table 3. Since we were only concerned with the trend of the adsorption energies, no zero-point energy corrections and basis set superposition error (BSSE) corrections were pursued.

(49) Wang, X. B.; Ding, C. F.; Wang, L. S. *J. Chem. Phys.* **1999**, *110*, 8217.

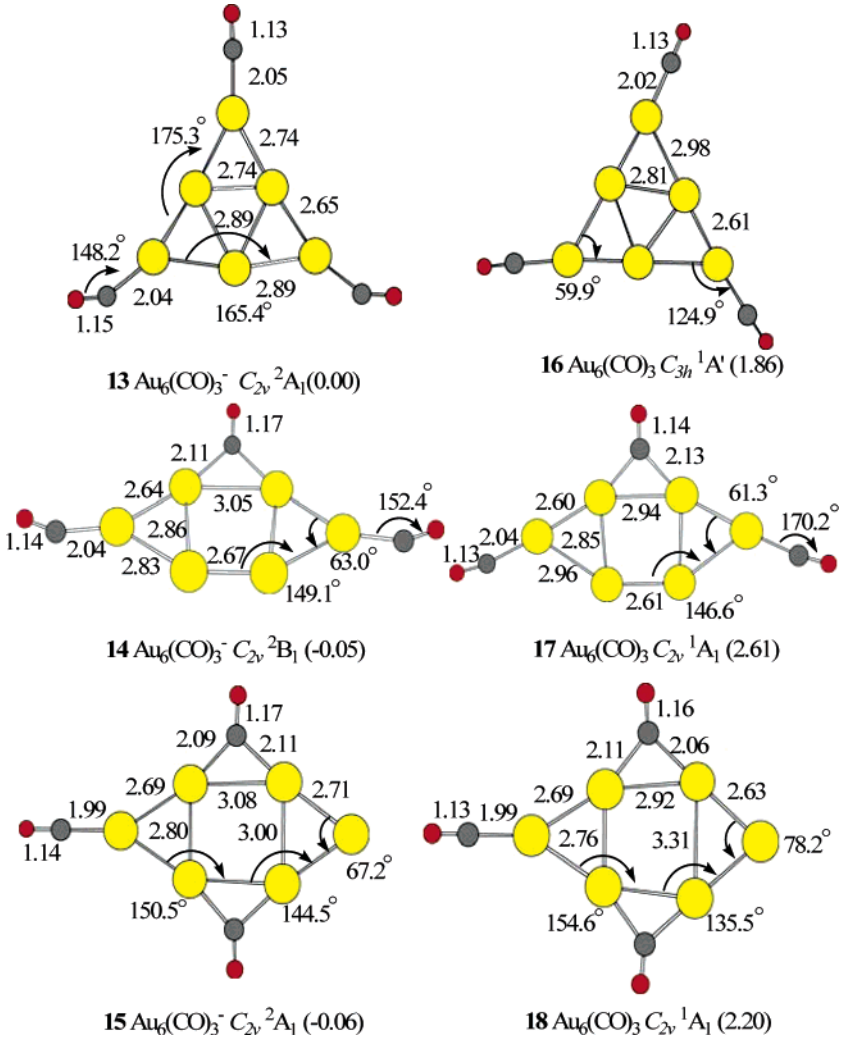


***Figure 4.*** Optimized structures of selected low-lying isomers of $Au_6(CO)_3^-$ and $Au_6(CO)_3$. All bond lengths are in Å, and all relative energies (in eV) are referenced to the anion ground state.

**4.1. $Au_6^-$ and $Au_6$.** The identified ground state (**1**) of $Au_6^-$ is $^2A_1'$ with one electron occupying the 6s-derived antibonding $a_1'$ orbital of $D_{3h}$ symmetry, in agreement with numerous previous theoretical calculations.[33,34,36] As shown in Figure 2, the structure (**1**) can be viewed as composed of an inner triangle made from the three edge atoms and an outer triangle made from the three apex atoms. The ground state of $Au_6$ (**3** $D_{3h}$ $^1A_1'$) is similar to the anion with some minor geometrical changes. In the anion ground state **1**, all Au−Au bond distances are almost equal, and the bond angle of the three edge atoms is almost linear (∠Au−Au−Au = 179.2°). Upon detachment of the extra electron, the inner triangle is slightly expanded while the outer triangle is slightly contracted because the extra electron is removed from the outer triangle. The anion-to-neutral structural changes from **1** to **3** can be understood from the LUMO of $Au_6$ or the singly occupied anion MO (SOMO $6a_1'$, Figure 6A), which is largely localized on the apex sites and exhibit weak bonding within the inner triangle and weak antibonding characters between the inner triangle and the apex atoms. We located a low-lying isomer for $Au_6^-$ (**2** $D_{2h}$ $^2A_g$, Figure 2), which was found to be only 0.30 eV higher in energy. The corresponding neutral $D_{2h}$ structure (**4**) was found to be 1.70 eV higher in energy.

**4.2. $Au_6(CO)^-$ and $Au_6(CO)$.** The ground state and a low-lying isomer for $Au_6(CO)^-$ and $Au_6(CO)$ are also given in Figure 2. The anion ground state **5** is $^2B_2$ with $C_{2v}$ symmetry, in which CO chemisorbs to an apex site of the triangular $Au_6^-$ cluster. The CO chemisorption results in a slight and interesting structural distortion in the $Au_6^-$ motif: the inner triangle is slightly expanded, and the overall shape of the $Au_6$ motif appears slightly elongated along the CO direction. A $C_{2v}$ ($^2B_2$) isomer **6** of $Au_6(CO)^-$, derived from the $D_{2h}$ isomer of $Au_6^-$ **2**, was found to be almost degenerate with the $C_{2v}$ ground state structure, only 0.03 eV higher in energy at the current level of theory. For neutral $Au_6(CO)$, the triangular structure **7** was found to be the ground state, whereas the $C_{2v}$ isomer **8** was found to be substantially higher in energy (by 0.99 eV). Our calculated CO chemisorption energy is 0.69 eV in $Au_6(CO)^-$ and 0.61 eV in the neutral complex (Table 3).

**4.3. $Au_6(CO)_2^-$ and $Au_6(CO)_2$.** The second CO also chemisorbs to an apex site on the triangular gold hexamer (Figure 3). The geometry of the $Au_6(CO)_2^-$ ground state (**9** $C_{2v}$ $^2A_1$) is similar to that of $Au_6(CO)^-$ **5**: the second CO appears to cause the two Au−Au bonds between the two chemisorption sites to lengthen. The only notable structural change between the ground state of $Au_6(CO)_2^-$ **9** and that of the neutral **11** is with respect

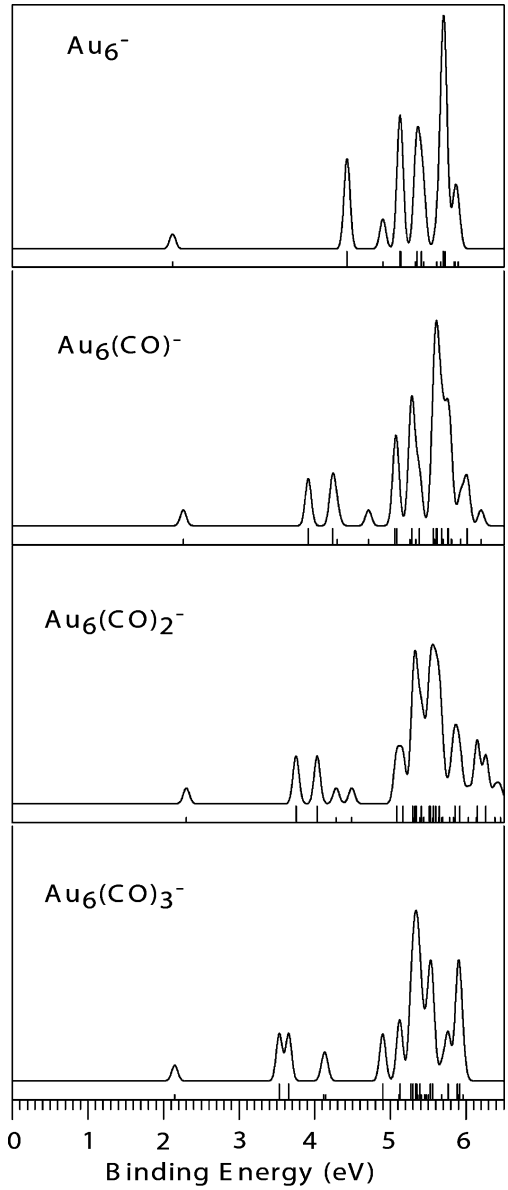


***Figure 5.*** Simulated photoelectron spectra for the ground-state structures of $Au_6(CO)_n^-$ ($n = 0-3$). The spectra were constructed by fitting the distribution of the calculated VDEs with unit-area Gaussian functions of 0.04 eV width.

***Table 3.*** Computed Average Chemisorption Energy per CO (in eV) in $Au_6(CO)_n^-$ and $Au_6(CO)_n$ ($n = 1-3$)[a]

| species | B3LYP[b,c] | PW91[c] |
|---|---|---|
| $Au_6(CO)^-$ | 0.69 | 0.98[d], 1.14[e] |
| $Au_6(CO)_2^-$ | 0.62 | 1.06[e] |
| $Au_6(CO)_3^-$ | 0.47 | 0.92[e] |
| $Au_6(CO)$ | 0.61 | 0.89[d] |
| $Au_6(CO)_2$ | 0.56 | |
| $Au_6(CO)_3$ | 0.53 | |

[a] All data are for optimized geometric structures based on the triangular $Au_6$ motif. [b] This work. [c] About 0.4−0.6 eV discrepancy between B3LYP and PW91 numbers was documented in ref 27. [d] From ref 27. [e] From ref 28.

to the ∠AuCO bond angle, which is 156.8° in the anion, but almost linear in the neutral structure. The $D_{2h}$ $Au_6$-based structure, **10** $C_s$ ($^2A'$), was found to be a low-lying isomer for $Au_6(CO)_2^-$ only 0.20 eV higher, where one CO adsorbs to a terminal site and the other on a bridging site. The neutral structure related to the $C_s$ isomer of the anion was found to be a low-lying isomer for neutral $Au_6(CO)_2$ **12**, which is 0.67 eV higher in energy than the triangular structure **11**. But the structure of this $Au_6(CO)_2$ isomer is completely distorted, in which one Au−Au bond is broken, leading to the low symmetry $C_s$ ($^1A'$) structure **12**. The chemisorption energy per CO in $Au_6(CO)_2^-$ and $Au_6(CO)_2$ decreases only slightly relative to the mono-CO chemisorbed systems (Table 3).

**4.4. $Au_6(CO)_3^-$ and $Au_6(CO)_3$.** Three anion structures (**13**−**15**) were identified for $Au_6(CO)_3^-$, which are energetically degenerate at the B3LYP level and cannot be differentiated without accurate account of the dispersion electron correlation effects. Their corresponding neutral structures (**16**−**18**) were also identified as minima. However, in the neutrals, the triangular $Au_6$-based structure $C_{3h}$ ($^1A'$) is clearly the ground state (**16**), with the $D_{2h}$ $Au_6$-based structures (**17** and **18**) being 0.75 and 0.34 eV higher, respectively. Note that structures **13** and **16** are significantly different in the CO chemisorption angles. Structure **13** is derived from the ground-state structure of $Au_6(CO)_2^-$ (**9**) by adsorbing a CO to the third apex site. In structure **16**, CO is almost collinear with one of the edges of the triangular $Au_6$, forming a propeller shaped $C_{3h}$ structure. Structures **14** and **15** are derived from the $D_{2h}$ isomers of $Au_6^-$ (**2**) with CO adsorbed at different positions. The chemisorption energy per CO in the triangular $Au_6(CO)_3^-$ (**13**) seemed to decrease slightly relative to that in $Au_6(CO)_2^-$, whereas in neutral $Au_6(CO)_3$ the per CO chemisorption energy is nearly the same as that in $Au_6(CO)_2$ (Table 3).

## 5. Discussion

**5.1. Comparison between the Experimental Data and Theoretical Calculations.** The calculated ADEs for the ground-state transitions, i.e., the electron affinities for neutral $Au_6(CO)_n$ ($n = 0-3$), are compared to the experimental values in Table 1. These values, computed from the differences between the total energies of the ground states of the anions and that of the neutrals, were all based on the triangular $Au_6$. Excellent agreement was observed between the calculated and experimental ADEs. For $Au_6(CO)_3^-$, there are three nearly degenerate structures competing for the ground state (Figure 4). However, only the triangular $Au_6$-derived structure (**13**) yielded an ADE that agrees with the experiment. The ADEs calculated for the two structures derived from the $D_{2h}$ $Au_6$ isomer (**14**, **15**) were both much higher than the experimental value because the corresponding neutrals were found to be significantly higher in energy than the triangular structure (Figure 4). The calculated VDEs from the triangular $Au_6$ derived ground-state $Au_6(CO)_n^-$ ($n = 0-3$) are also in excellent agreement with the experiment (Table 1).

The computed reorganization energies are compared with the experimental values in Table 2. Excellent agreement was also observed. The relatively small values of the reorganization energies are consistent with the small geometrical changes between the anion and the neutral ground states from the triangular $Au_6$ derived complexes (Figures 2−4). The largest reorganization energy was for the three CO chemisorbed complex, largely due to the CO bond angle changes between the anion **13** and the neutral **16** (Figure 4).

The calculated VDEs for the first excited state of neutral $Au_6(CO)_n$ ($n = 0-3$) are also compared with the experimental

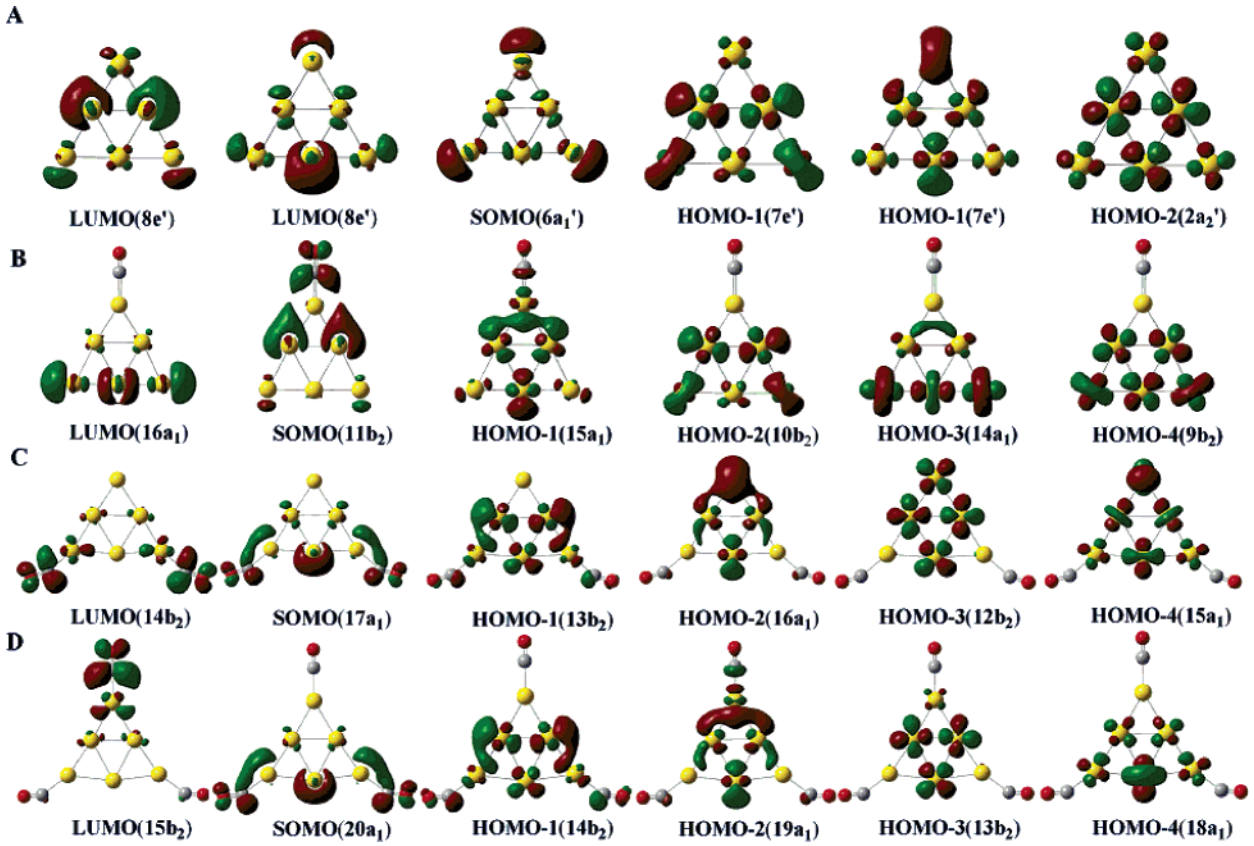


***Figure 6.*** Molecular orbital pictures of (A) $Au_6^-$, (B) $Au_6(CO)^-$, (C) $Au_6(CO)_2^-$, and (D) $Au_6(CO)_3^-$.

values in Table 1. The theoretical results are in perfect agreement with the experiment. The difference between the VDEs of the first excited state and of the ground-state detachment transitions defines the X−A energy gap, an approximate measure of the HOMO−LUMO gap of the neutral complexes. We see from Table 2 that the computed HOMO−LUMO gaps agree very well with the experimental values. In particular, the large HOMO−LUMO gap of $Au_6$ was well reproduced, as well as the trend of the decreasing gaps in the $Au_6(CO)_n$ complexes with increasing CO chemisorption.

The PES spectra beyond the first excited-state become much more complicated with a very high density of electronic states. We also computed VDEs for the higher detachment channels up to the 193 nm photon energy. Numerical values are given in Tables S1−S4 for $Au_6(CO)_n^-$ ($n = 0-3$), respectively. Simulated spectra based on the computed VDEs are shown in Figure 5. The simulated spectra agree qualitatively with the experimental spectra (Figure 1). As discussed above, the first two detachment transitions, as well as the trend of the energy gap, reproduced well the experimental observation. The weak signals observed in the HOMO−LUMO gap region in the experimental spectra of the chemisorbed complexes (Figure 1) were most likely due to the $D_{2h}$ $Au_6^-$ derived isomers. The computed ADEs and VDEs for these isomers (Tables S2−S4) agree with the experimental observation.

**5.2. Electronic Structure and Chemical Bonding in $Au_6$.** Before the discussion of the chemical interactions between $Au_6$ and CO, it is instructive to examine the bare $Au_6$ neutral. The bonding in $Au_6$ can be understood by mainly considering the orbital interactions of the Au $6s^1$ electrons; the Au $5d^{10}$ manifold can be qualitatively viewed as being simply broadened upon

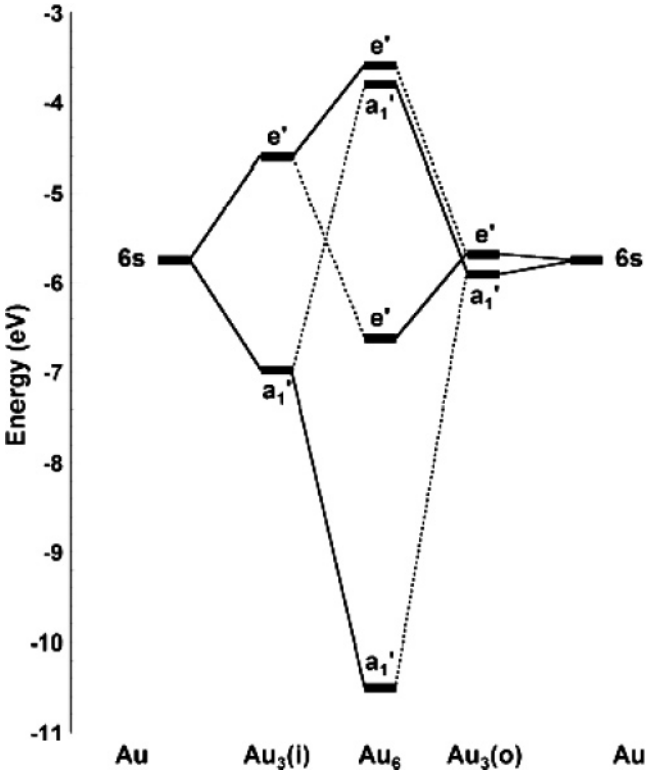


***Figure 7.*** Orbital interaction diagram for $Au_6$. $Au_3$(i) and $Au_3$(o) represent the inner and outer triangles, respectively, for the $D_{3h}$ $Au_6$ (**1** in Figure 2). Only one of the three degenerate Au 6s orbitals is shown at the far-left and far-right.

orbital overlap. As shown in Figure 7, the 6s orbitals of the inner $Au_3$(i) and outer $Au_3$(o) triangles in $Au_6$ both form $a_1' +$

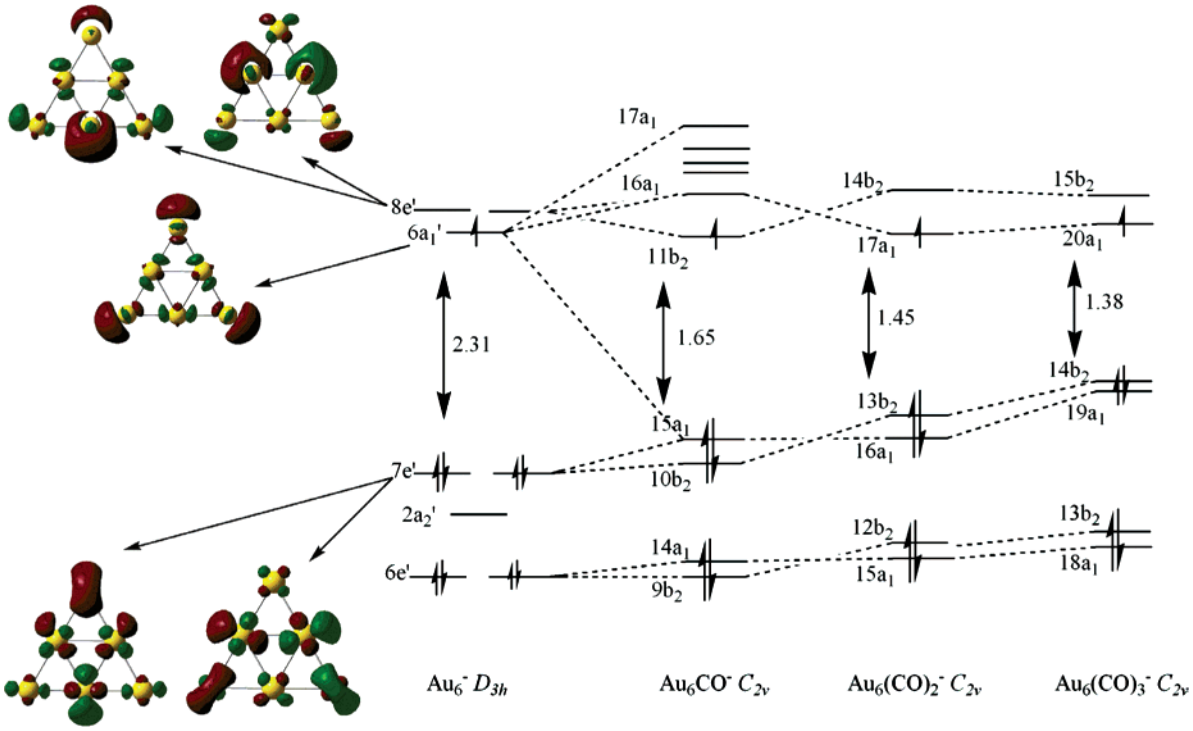


***Figure 8.*** Schematic energy level diagrams of $Au_6(CO)_n^-$ ($n = 0-3$) based on TD-DFT calculations.

e′ representations. The orbital interaction between the inner and outer $Au_3$ fragments leads to the formation of a bonding and antibonding pair of $a_1' + e'$. The six $6s^1$ electrons fully occupy the $a_1' + e'$ bonding orbitals, giving rise to a $(a_1')^2(e')^4(a_1')^0(e')^0$ electron configuration, which is analogous to the delocalized $\pi$ electrons in benzene. The antibonding $a_1' + e'$ orbitals, which are nearly degenerate, are unoccupied and become the LUMO and LUMO+1, respectively (Figure 7). This unique electron configuration and the delocalized nature of the $a_1' + e'$ orbitals render $Au_6$ a highly $\sigma$-aromatic system, explaining its special stability and its extremely large HOMO−LUMO gap. As shown in Figure 6A, the $a_1'$ LUMO of $Au_6$ (the $6a_1'$ SOMO in $Au_6^-$) is mainly from the outer $Au_3$ fragment, whereas the e′ LUMO+1 orbitals (8e′) are mainly from the inner $Au_3$ fragment. The different spatial distributions of these orbitals and their near degeneracy turn out to be the key in understanding the interaction of $Au_6$ and CO.

**5.3. Electronic Structure Evolution and Chemical Bonding in $Au_6(CO)_n^-$.** As noted above, there are two major surprising experimental observations for CO interacting with $Au_6^-$. In contrast to the smaller gold clusters, chemisorptions of CO on $Au_6^-$ do not alter significantly the electron binding energies in the $Au_6(CO)_n^-$ complexes, whereas the X−A band gap decreases continuously with increasing CO chemisorption (Figure 1). This indicates that the LUMO of the neutral $Au_6(CO)_n$ complexes, into which the extra electron occupies in the anions, is energetically not affected by the CO chemisorption, while the HOMO is pushed up in energy. These observations can be understood from the above MO analysis for $Au_6$ and the schematic MO level diagram depicted in Figure 8. The HOMO of $Au_6$ is the degenerate 7e′ orbitals (Figure 6A), which involve strong s−d hybridization and are highly delocalized. The LUMO of $Au_6$ is $6a_1'$ (Figure 6A), which is mainly distributed on the three apex atoms (outer triangle). In the $Au_6^-$ anion the extra electron enters the $6a_1'$ orbital and the charge is distributed on the outer triangle. What is unique to $Au_6$ is that its LUMO+1 (8e′) (Figure 6A), which is mainly concentrated on the inner triangle, is very close in energy to the LUMO, as shown in Figure 8. The consequence of this energetic proximity between the LUMO and LUMO+1 in $Au_6$ will become clear when CO is adsorbed.

When one CO is coordinated to an apex atom of $Au_6$, the symmetry of the molecule is lowered from $D_{3h}$ to $C_{2v}$, and the degenerate LUMO+1 (8e′) of $Au_6$ is split into $a_1$ and $b_2$ orbitals. The $a_1$ component of the 8e′ orbital strongly mixes with the $6a_1'$orbital, which are both destabilized (Figure 8). On the other hand, the $b_2$ component of the 8e′ orbital interacting with the CO $2\pi$ orbitals becomes the LUMO, into which the extra electron enters in $Au_6(CO)^-$. Consequently, the CO chemisorption to $Au_6^-$ induces an internal electron transfer from the outer triangle to the inner triangle. Since the $b_2$ LUMO of $Au_6CO$ ($11b_2$) does not change much energetically relative to that in the bare $Au_6$ species, similar electron binding energies are expected for the two systems. In $Au_6(CO)_2^-$ and $Au_6(CO)_3^-$, the $a_1$ component of the 8e′ orbital becomes the LUMO, which is again localized on the inner triangle (Figure 6) and whose binding energy is not expected to change significantly relative to that of $Au_6^-$. This situation is unique to the $D_{3h}$ $Au_6$ structure, where there exist two spatially distinct but energetically similar regions in the molecule. Thus, in the anions, the extra electron shuttles from the outer triangle to the inner triangle upon chemisorption, resulting in a relatively constant electron binding energy for the SOMO in both $Au_6^-$ and $Au_6(CO)_n^-$ ($n = 1-3$) (Figure 8). In other words, since the extra electron in $Au_6(CO)_n^-$ ($n = 1-3$) is localized on the inner Au atoms, it is not sensitive to the CO chemisorption, which only involves the outer Au atoms. This is also reflected in the similar CO binding energies between the $Au_6(CO)_n$ neutrals and the $Au_6(CO)_n^-$ anions and their relative independence of the CO numbers (Table 3).

The CO chemisorption also lifts the degeneracy of the 7e′ HOMO of the $D_{3h}$ $Au_6$, forming $a_1$ and $b_2$ orbitals under the $C_{2v}$ symmetry in $Au_6(CO)_n$. The $a_1$ or $b_2$ orbital from the HOMO mixes with the corresponding orbital from the LUMO, pushing up the HOMO level in the chemisorbed complexes, $15a_1$ for $n = 1$, $13b_2$ for $n = 2$, and $14b_2$ for $n = 3$ (Figure 8). The destabilization of the HOMO in the chemisorbed systems is further enhanced by the CO 5$\sigma$-donation, which is repulsive due to closed-shell/closed-shell interactions. The relatively constant LUMO level plus the destabilization of the HOMO level in $Au_6(CO)_n$ gives rise to the decreasing band gaps observed in the chemisorbed complexes.

The large HOMO−LUMO gap in $Au_6$ arises from the $\sigma$-aromaticity of the $Au_6$ 6s manifold. Accordingly, the $Au_6$ cluster is quite inert chemically, and it is known not to be reactive to $O_2$. The destabilization of its HOMO upon CO chemisorption provides an important activation mechanism. Thus it is expected that neutral chemisorbed $Au_6(CO)_n$ complexes should be reactive toward $O_2$. This cooperative chemisorption behavior seems to be an essential feature in considering the catalytic mechanisms of nanogold for CO oxidation.

## 6. Conclusions

We report a combined photoelectron spectroscopic and theoretical investigation of $Au_6(CO)_n^-$ ($n = 0-3$). Photoelectron spectra were obtained at several photon energies and revealed surprisingly that the electron affinities of $Au_6(CO)_n$ are relatively independent of the CO chemisorption, whereas the HOMO−LUMO gap decreases with CO chemisorption. Extensive density functional calculations were carried out, showing that CO prefers to bind to the apex sites of the triangular $Au_6$ in both $Au_6(CO)_n$ and $Au_6(CO)_n^-$ ($n = 1-3$). The experimental observation was elucidated through molecular orbital analyses, yielding detailed information about the molecular interactions between CO and $Au_6$. The unique triangular structure of $Au_6$ is responsible for the surprising experimental observation. It turns out that the LUMO ($6a_1'$) and LUMO+1 (8e′) of $Au_6$ are nearly degenerate and they are localized on the outer and inner $Au_3$ triangles of the $D_{3h}$ $Au_6$, respectively. Upon CO chemisorption, the symmetry of the chemisorbed complexes is lowered and the degeneracy of the LUMO+1 is lifted. One component of the LUMO+1 orbital in $Au_6$ becomes the LUMO in the $Au_6(CO)_n$ complexes. Since the LUMO in the $Au_6(CO)_n$ complexes is mainly localized in the inner triangle of the $Au_6$ substrate, it is not affected energetically by the CO chemisorption; i.e., an electron shuttling from the outer triangle to the inner triangle takes place upon CO chemisorption in the negatively charged systems. On the other hand, the HOMO of $Au_6$ is destabilized upon CO chemisorption due to both HOMO−LUMO orbital interactions and the CO 5$\sigma$-donation, causing the decreasing HOMO−LUMO gap. This series of complexes thus provides ideal molecular models of nanogold catalysts for CO oxidation. The destabilization of the HOMO of $Au_6$ upon CO chemisorption should promote reactions with $O_2$, providing a mechanism for cooperative chemisorption and catalytic reactions.

**Acknowledgment.** This work was supported by the National Science Foundation (CHE-0349426) and performed at the W. R. Wiley Environmental Molecular Sciences Laboratory (EMSL), a national scientific user facility sponsored by the Department of Energy's Office of Biological and Environmental Research and located at the Pacific Northwest National Laboratory, operated for DOE by Battelle. All calculations were performed with supercomputers at the EMSL Molecular Science Computing Facility.

**Supporting Information Available:** The complete sets of photoelectron spectra for $Au_6(CO)_n^-$ ($n = 0-3$) at 532, 266, and 193 nm, experimental and theoretical electron detachment energies, and alternative structures optimized for the anions and neutrals along with their relative energies. This material is available free of charge via the Internet at http://pubs.acs.org.

JA052618K